

X-ray Imaging with ePix100a, a High-Speed, High-Resolution, Low-Noise Camera

G. Blaj^a, P. Caragiulo^a, A. Dragone^a, G. Haller^a, J. Hasi^a, C.J. Kenney^a, M. Kwiatkowski^a,
B. Markovic^a, J. Segal^a, A. Tomada^a

^aSLAC National Accelerator Laboratory, 2575 Sand Hill Road, Menlo Park, CA 94025, U.S.A.

ABSTRACT

The ePix100A camera is a 0.5 megapixel (704×768 pixels) camera for low noise x-ray detection applications requiring high spatial and spectral resolution. The camera is built around a hybrid pixel detector consisting of 4 ePix100a ASICs flip-chip bonded to one sensor. The pixels are $50 \mu\text{m} \times 50 \mu\text{m}$ (active sensor size $\sim 35.4 \text{ mm} \times 38.6 \text{ mm}$), with a noise of $\sim 180 \text{ eV rms}$, a range of 100 8 keV photons, and a current frame rate of 240 Hz (with an upgrade path towards $\sim 10 \text{ kHz}$). This performance leads to a camera combining a high dynamic range, high signal to noise ratio, high speed and excellent linearity and spectroscopic performance. While the ePix100A ASIC has been developed for pulsed source applications (e.g., free-electron lasers), it performs well with more common sources (e.g., x-ray tubes, synchrotron radiation). Several cameras have been produced and characterized and the results are reported here, along with x-ray imaging applications demonstrating the camera performance.

Keywords: ePix, spectroscopic x-ray imaging, hybrid pixel detector, high speed, high dynamic range, high resolution, high linearity, photon counting

1. INTRODUCTION

The ePix100a cameras are x-ray imaging cameras initially designed for applications at pulsed sources, e.g., free-electron lasers (FELs). They are developed on the ePix platform^{1,2} and are optimized for low noise, high spatial resolution and fast frame rates.³ Currently there are 7 ePix100a cameras (3.6 Mpixel) deployed at LCLS. Camera performance with pulsed sources has been briefly described elsewhere.^{4,5}

While initially designed for use at pulsed sources, the ePix100a will be upgraded allowing much faster frame rates,⁶ opening new possibilities in x-ray imaging with more conventional light sources. This paper concentrates on characterisation of the ePix100a camera and imaging performance with continuous sources (i.e., x-ray tubes).

2. MATERIALS AND METHODS

2.1 ePix100a Camera

The ePix100a cameras are built around hybrid pixel detector modules consisting of 4 ePix100a ASICs flip-chip bonded to one monolithic Si sensor with a thickness of $300 \mu\text{m}$ and a size of $35.4 \text{ mm} \times 39.1 \text{ mm}$. The pixel size is $50 \mu\text{m} \times 50 \mu\text{m}$, with one detector module containing $704 \text{ pixel} \times 768 \text{ pixel}$ (0.54 Mpixel). Each pixel has a range of 100 8 keV x-ray photons and noise of 50 e^- . The camera currently operates at 240 Hz, with an upgrade path towards 10 kHz.⁶ The mechanical package is very compact ($155 \text{ mm} \times 52 \text{ mm} \times 52 \text{ mm}$), 4-side buttable, vacuum compatible, and EMP-resistant; for an overview of the camera mechanical and electronic design, see Ref. 7.

The camera can operate in different modes as shown in Table 1: power pulsing on (reduced energy and heat dissipation, slightly increased noise level) or off, temperature compensation on or off; we tested all 4 combinations. In post-processing, the common mode noise can be corrected using block, block and row, column and row, or no correction as shown in Table 2. (There are 16 readout blocks with 96 half-columns each, as shown in Ref. 3).

Measurements were performed while precisely controlling the camera head (i.e., detector module) with the incorporated Peltier element driven by a Thorlabs TED4015 temperature controller, while the camera body was maintained at 15°C using chilled water supplied by a ThermoCube 400 chiller from Solid State Cooling Systems. Throughout the experiments, the camera was flushed with dry nitrogen.

Corresponding author: blaj@slac.stanford.edu
SLAC-PUB-16777

Table 1. ePix100 operation modes

Acronym	Off	TC*	PP	PP & TC
Power Pulsing	Off	Off	On	On
Temperature Compensation	Off	On	Off	On

Table 2. ePix100 common mode correction settings

Acronym	Off	B*	B & R	C & R
Common mode correction:	none	block level	block and row level	column and row level

2.2 X-ray Imaging Setup

We used an X-Beam x-ray tube system from Xray Optical Systems Inc., based on a microfocus x-ray tube with molybdenum anode. For gain calibration and imaging with quasi-monochromatic MoK α radiation, the x-ray tube was operated at 27 kV, with 200 μ m Zr and 500 μ m Al filters to preferentially remove energies above and below the Mo K α lines. The filters were placed very close to the x-ray tube and the camera was placed 0.3 m away to reduce the influence of filter fluorescence and scattering. For spectroscopic imaging, a full spectrum including bremsstrahlung was used.

2.3 X-ray Transport Simulations

Simulations were performed with PENELOPE 2011,⁸ distributed by OECD/Nuclear Energy Agency Data Bank (Paris) and the RSICC at Oak Ridge National Laboratory.

3. CAMERA PERFORMANCE

3.1 Noise

Noise measurements were acquired using different combinations of temperature, operating parameters (integration time, power pulsing, temperature compensation), and post-processing common mode noise correction settings.

Fig. 1 shows the dark map (average of 1024 frames) and the noise map (r.m.s of 1024 frames with block common mode correction - relevant for low signals) of a data set measured in standard conditions: fully biased sensor 200 V, 50 μ s integration time, power pulsing off, and temperature compensation on (TC). Both the dark and the noise maps are uniform with a low noise, under 3 analog-to-digital units (adu) in the data set shown. As we will show further, 1 adu is equivalent to a signal of ~ 54 eV, or ~ 15 e $^-$.

A summary of multiple noise data sets (including the one shown in Fig. 1) is presented in Fig. 2, measured in different operating modes, with different integration times, at different temperatures and with different post-processing common mode approaches.

Fig. 2(a) shows a histogram of the data in Fig. 1 and compares the raw noise, which is relevant for high photon occupancy and large signals, with the block common mode corrected noise, relevant for small signals and low photon occupancy. Fig. 2(b) summarizes the median photon noise over all four common mode approaches and 2 integration times; block common mode is robust and accurate, making it a good default for low photon occupancy frames.

In subsequent figures, the default (or standard) configurations will be denoted by a star (*). The standard configuration leads to a noise of 2.75 adu; with the gain 54 eV/adu, the absolute noise level is 149 eV, or 41 e $^-$.

Currently, analog signals are shipped off the ASICs to ADC converters, limiting the readout speed and increasing the interference inducing common mode noise; both will be improved with on-chip ADC parallel digitisation.⁶

Fig. 2(c) summarizes the median photon noise over two different temperatures (-10°C and 5°C) and integration times. The temperature has little effect on noise. Longer integration times increase the noise somewhat

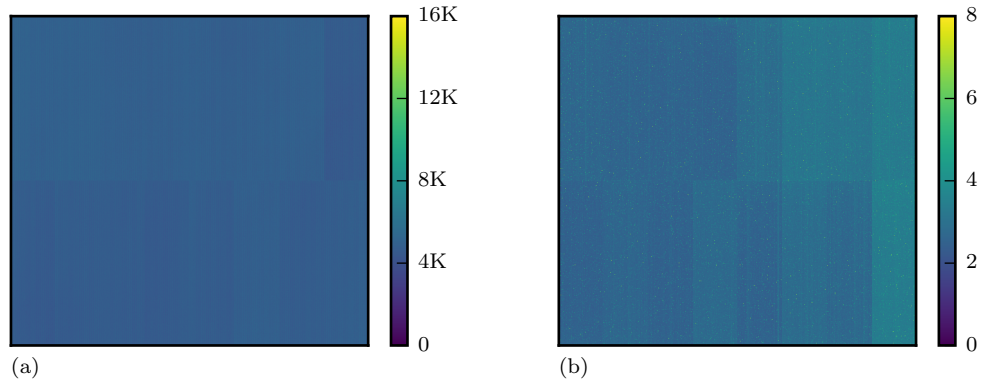


Figure 1. Dark and noise maps of a camera with fully biased sensor (200 V) and an integration time of 50 μ s, with standard configuration (temperature compensation on, TC) and calculated over 1024 frames; (a) dark map (average), showing good uniformity; (b) corresponding noise map (root mean square, rms) showing very low noise and good uniformity.

(note the y scale). Fig. 2(d) summarizes the median photon noise over two different integration times and four operating modes: with long integration times, the power pulsing mode shows a somewhat increased noise while with short integration times there is little difference.

3.2 Gain

Pixel gain calibration was performed with low occupancy, quasi-monochromatic radiation obtained with an x-ray tube with molybdenum anode. To optimize the beam parameters, the tube was operated at 27 keV, and the resulting spectrum was filtered with 200 μ m Zr and 500 μ m Al. A Monte Carlo simulation of the characteristic Mo spectrum and the result of filtering are shown in Fig. 3. Briefly, before filtering, the x-ray beam is clearly not monochromatic, with the average photon energy and standard deviation are 8041 eV and 5805 eV, respectively.

After filtering, the average and standard deviation become 17 033 eV and 1231 eV, respectively. The average is relevant for the absolute gain calibration while the standard deviation of the beam photon energy (1231 eV) is relevant for the beam widening noise calculation. With these beam parameters, the standard deviation of the photon energy will add quadratically with the actual detector noise, becoming the dominant factor in detected peak width.

We performed gain calibrations in different conditions by acquiring from 33 000 to 220 000 frames with low occupancy, quasi-monochromatic radiation as described above. We defined "single pixel events" as photon detection events where most of the photon charge has been deposited in one pixel and all 8 neighboring pixels were within the noise ($< 6 \sigma$).

Each pixel gain was calculated by accumulating only single pixel events, summing up their charge and dividing it by the number of single pixel events. Fig. 4(a) shows the resulting gain map for standard parameters and Fig. 4(b) shows the corresponding histogram. Careful investigation of the gain map and of spectra of individual gain-corrected pixels showed that the gain calculation method is suboptimal (with individual pixel gains scattered around the actual gain, visible in suboptimal alignment of peaks in individual pixel spectra).

However, the population mean is accurate, leading to a gain factor of $17\,033/314.6 \text{ adu} = 54.14 \text{ eV/adu}$, equivalent with $15.04 \text{ e}^-/\text{adu}$. The gain variation (root mean square, rms) at 5.7 adu is overestimated; however, it establishes an upper limit to the gain variation of 1.8%.

Fig. 5(a) compares 2 different gain maps, with the 2 gains of each pixel represented by a dot. Individual pixel gain estimations are somewhat noisy, however, the population of pixels suggests there is good agreement between the 2 sets (slope ~ 1 , intercept ~ 0).

Extending the gain comparison to different operation modes and integration times in Fig. 5(b) we obtained small variations of less than 1%. The gains appear to be consistent across measurements in different conditions.

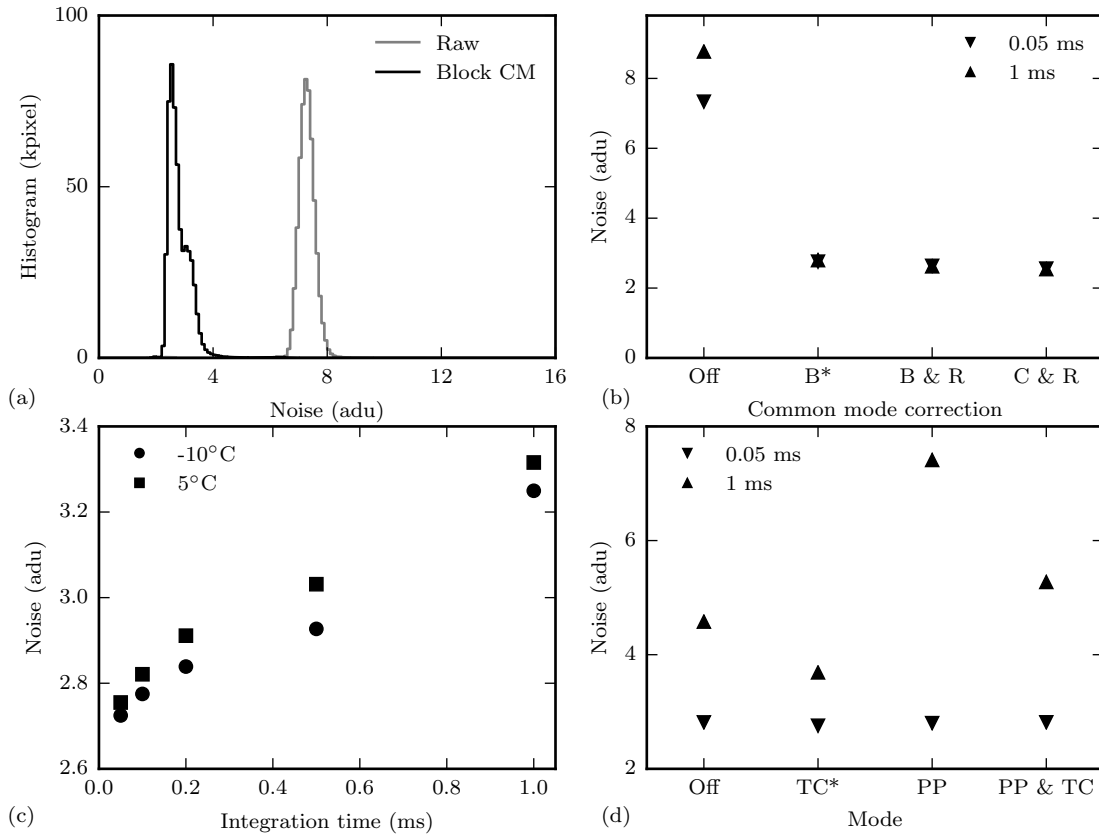


Figure 2. Noise statistics (rms of 1024 frames) in different operating modes, integration times, temperatures and common mode correction approaches; (a) noise histograms in standard configuration (TC), with the raw noise (gray, relevant for large signals or high occupancy) and block common mode correction (black, relevant for small signals and low occupancy); (b) effect of different common mode and integration times, showing block common mode correction performing adequately; (c) detector temperature has little influence on camera noise, while integration time has limited impact (note y axis scale); (d) with long integration times, the power pulsing mode shows a somewhat increased noise while with short integration times there is little difference.

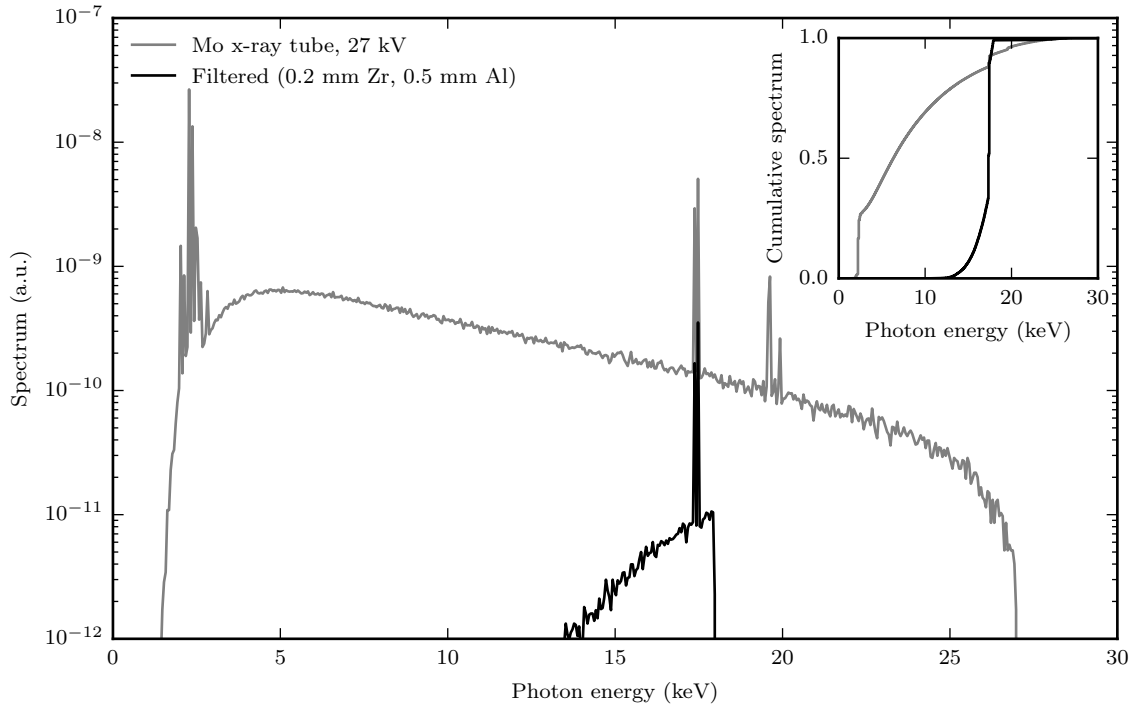


Figure 3. Monte Carlo simulation of the optimized parameters for a quasi-monochromatic beam; figure shows a characteristic spectrum of a x-ray tube with Mo anode at 27 keV (gray) and after filtering (black); inset shows the corresponding cumulative spectra, normalized to 1: before filtering, $\sim 5\%$ of the photons are around the Mo $K\alpha$ lines; after filtering, $\sim 50\%$; photon energy statistics before filtering: $8041\text{ eV} \pm 5805\text{ eV}$ and after filtering: $17033\text{ eV} \pm 1231\text{ eV}$; note that the 1231 eV rms will make peaks appear wider than with monochromatic radiation.

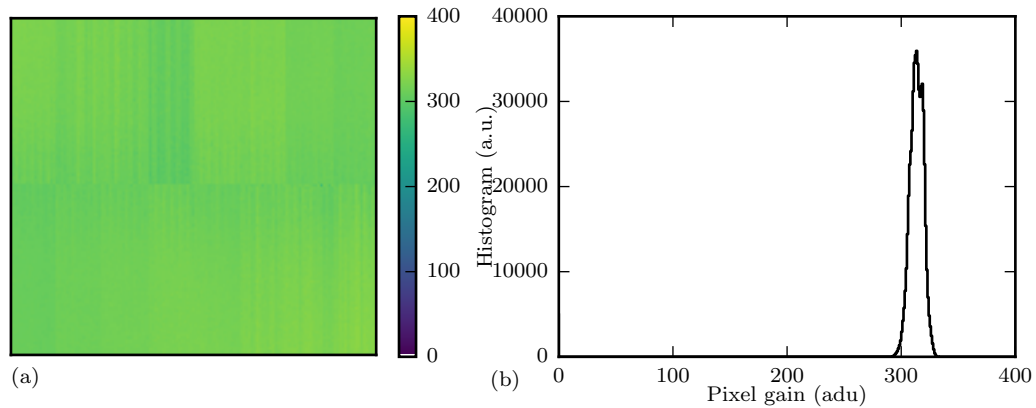


Figure 4. Gain calculated for standard settings and integration time of $50\ \mu\text{s}$; (a) gain map, showing the average pixel values (in adu) corresponding to the average photon energy; a structure is apparent, however, inspection of individual gain-corrected pixel spectra reveal that the current fast gain calibration is suboptimal; (b) histogram of (suboptimal) gain map: $314.6\text{ adu} \pm 5.7\text{ adu}$, establishing an upper limit for the actual gain variation.

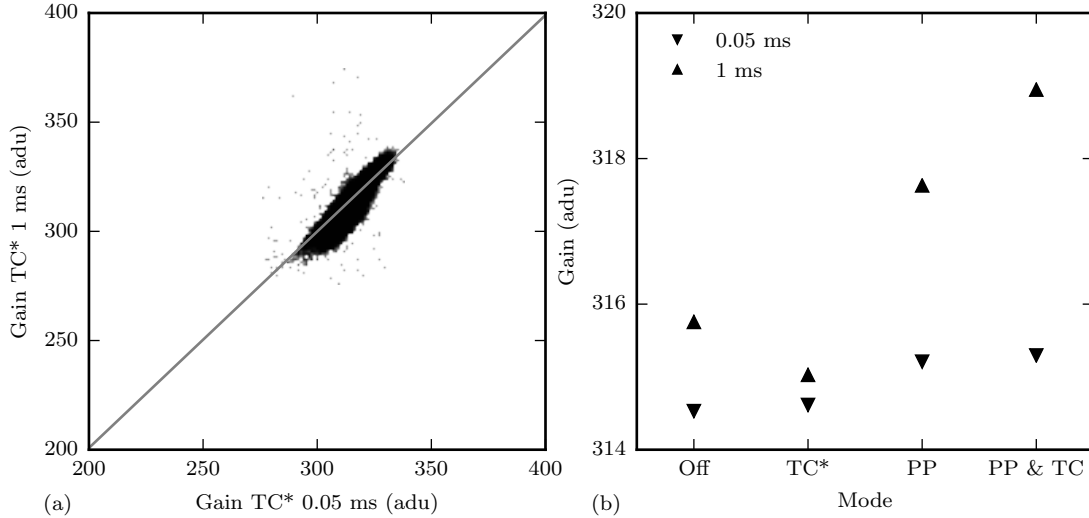


Figure 5. Comparison of gain maps with different operating modes and integration times; (a) 2 gain maps with standard parameters (temperature compensation on) where each dot represents the 2 gains of individual pixels and the gray line is a linear fit; individual gain estimations are noisy, while the correspondence is good (slope ~ 1 , intercept ~ 0); (b) the median gain in different operating modes and integration times; differences are less than 1% (note y scale).

3.3 Signal to Noise Ratio

The noise and gain measurements above show that the camera noise is very low at 149 eV; for 8 keV photons the signal to noise ratio (SNR) is ~ 53.7 . In Ref. 5, Fig. 3 shows an example of a histogram obtained with a monochromatic 7 keV FEL beam, where individual peaks for 1 to 64 photons are clearly separated.

The operating parameters have little influence on the gain. However, the noise can change. In the least favorable configuration, the noise would be ~ 9 adu, corresponding to a SNR of ~ 16.4 .

The minimum detectable signal is $\sim 3\sigma$, corresponding to 448 eV. Signals from photons that can be comfortably counted, including pile-up, start from 1.49 keV.

Often a droplet charge reconstruction algorithm is used, collecting individual events shared between 4 neighboring pixels, summing their total charge, and assigning it to the pixel with the highest signal. This results in a noise level two times larger but it virtually eliminates charge sharing thus improving spectroscopic performance.

3.4 Flat Field and Spectral Resolution

Fig. 6 shows the flat field calculated on the same data and with the same (suboptimal) algorithm as in Fig. 4; in this data set there are on average $\sim 270 \pm 21.9$ photons per pixel.

The corresponding spectrum calculated from the energies of the individual photons is displayed in Fig. 7 and is similar to the simulated spectrum in Fig. 3; the spectral broadening is compatible with the expected detector response function (full width at half maximum of $2.634 \times 149 \text{ eV} \sim 400 \text{ eV}$). Additionally, there are several fluorescence lines visible at low energies, as well as the broad continuum in the left flank.

3.5 Quantum Efficiency

An essential component of x-ray imaging at different energies is the energy-dependent detective quantum efficiency (DQE). We simulated the current ePix sensor 300 μm silicon, a doped (non-detective) silicon layer of 3 μm and an additional aluminum entrance window of 1 μm . The results are presented in Fig. 6.

The entrance window reduces DQE at low energies (see inset). However, the system performs well right under the Si K absorption edge (1.839 keV), and especially under the Al K absorption edge (1.560 keV). At these

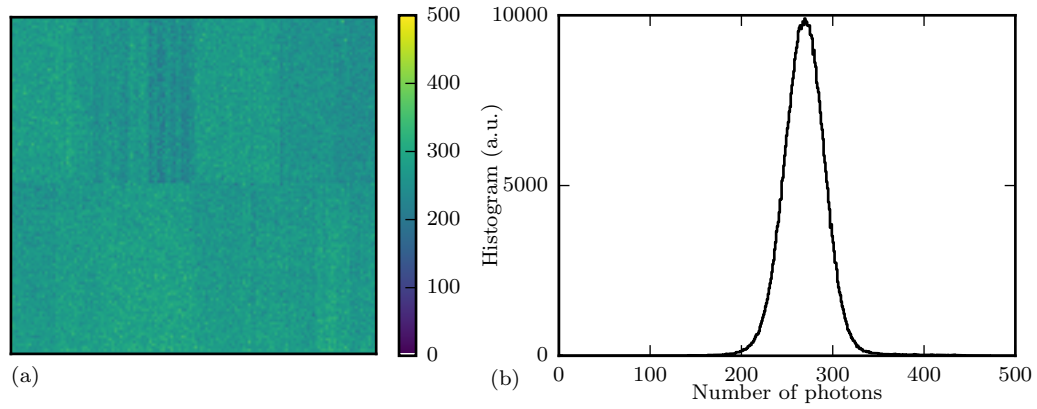


Figure 6. Flat field calculated on the same data used in Fig. 4; (a) shows the flat field map which is somewhat nonuniform due to suboptimal gain and flat field calculation; (b) shows the corresponding histogram, showing 270.0 ± 21.9 photons/pixel.

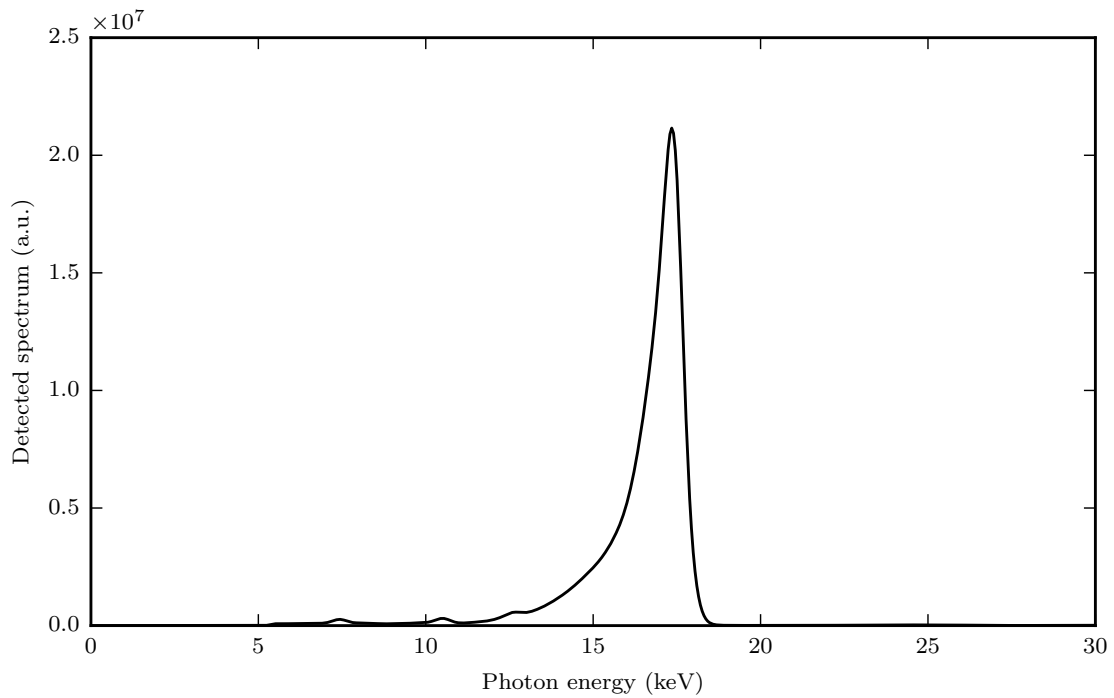


Figure 7. X-ray tube spectrum, detected by the ePix100a camera. The detected spectrum is similar to the simulated spectrum in Fig. 3. Additionally, there are several fluorescence lines visible at low energies.

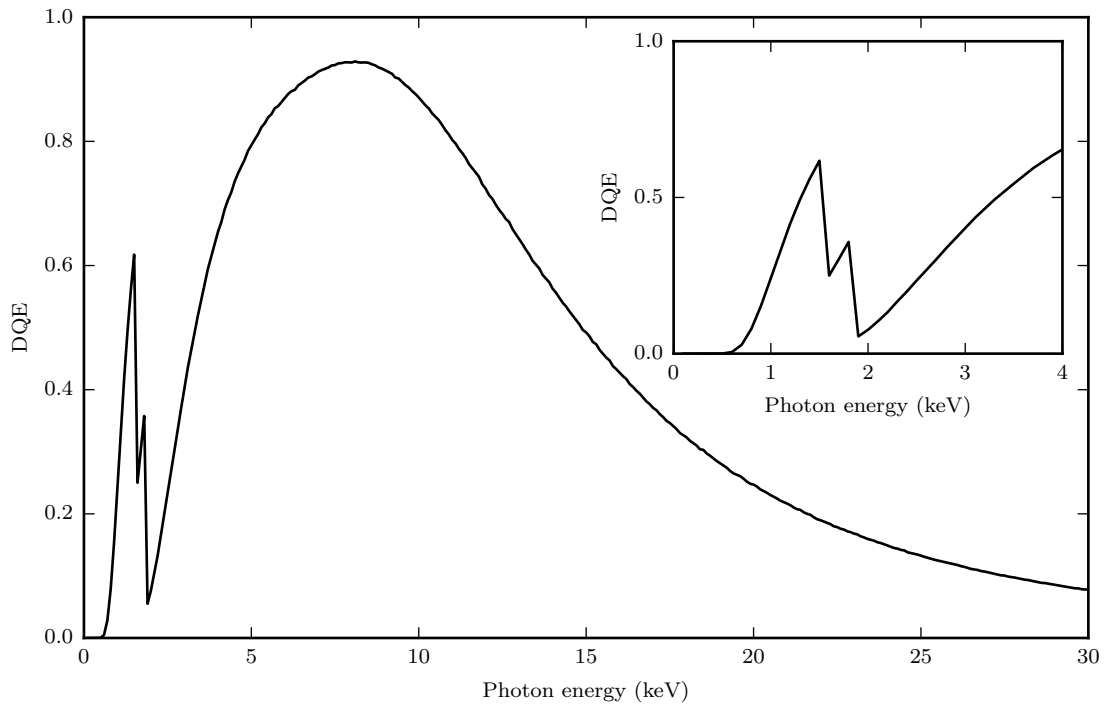


Figure 8. Monte Carlo simulation of the detective quantum efficiency (DQE) for a standard Si sensor (300 μm thick, with standard entrance window), showing excellent performance around 8 keV and reasonable performance in the range of 3 keV to 25 keV; a thicker sensor would improve somewhat the DQE at high energies, however, charge sharing would also increase; the inset shows a close-up at low energies, with a reasonable DQE in the range of ~ 1 keV to 1.8389 keV (Si K absorption edge), well above the camera noise level ($\sigma=149$ eV); a thin entrance window would significantly improve the DQE at low energies.

energies, the effective SNR is ~ 10 (for details, see 'Gain' subsection above). Note that a thin entrance window would greatly improve the DQE at low energies. Towards high energies (over 16 keV), the DQE drops quickly; a thicker Si sensor offers diminishing returns at higher energies.

3.6 Linearity and Range

ePix100a are integrating detectors thus avoiding⁴ the photon counting non-linearity⁹ at high intensities and/or high photon bunching. Even when photons arrive quasi-simultaneously (within femtoseconds), the low noise (and corresponding SNR) allows photon counting, as shown in Fig. 3 of Ref. 5 (where a histogram of detected 7 keV photons shows clearly separable peaks from 1 to 64 photons).

The current version of the ePix100a operates at 240 Hz and individual pixels have ranges of ~ 100 8 keV photons, thus allowing the acquisition of $\sim 20\,000$ photons pixel⁻¹ s⁻¹.

The ePix100a cameras are being upgraded to much higher frame rates, towards 10 kHz.⁶ This will allow acquisition of individual photons at speeds currently accessible to spectroscopic photon counting detectors^{10,11} while additionally preserving the full linear, spectroscopic (low noise) and sub-pixel information for each individual photon.

4. CONCLUSIONS

The x-ray imaging performance of the ePix100a camera has been described in detail, with an emphasis on x-ray tube light sources. The noise level is low (149 eV rms), allowing high SNR measurements. The gain calibration algorithm is being improved.

Imaging with monochromatic radiation allows precise photon counting of up to $\sim 20\,000$ photons pixel⁻¹ s⁻¹ with good linearity. When imaging with a complex spectrum and low photon occupancy, x-ray K edge imaging is possible. X-ray spectroscopy with a full width at half maximum of ~ 500 eV is also possible.

The ePix100a cameras are being upgraded to much higher frame rates, towards 10 kHz. The higher speeds will allow fast and accurate acquisition of the entire spectroscopic and (sub-pixel) positional information with very low noise.

ACKNOWLEDGMENTS

This work was supported in part by the U.S. Department of Energy under DOE Contract DE-AC02-76SF00515.

REFERENCES

- [1] Dragone, A., Caragiulo, P., Markovic, B., Herbst, R., Nishimura, K., Reese, B., Herrmann, S., Hart, P. A., Blaj, G., Segal, J., Tomada, A., Hasi, J., Carini, G., Kenney, C., and Haller, G., "ePix: a class of front-end ASICs for second generation LCLS integrating hybrid pixel detectors," in [2013 IEEE Nuclear Science Symposium and Medical Imaging Conference (2013 NSS/MIC)], 1–5, IEEE (Oct 2013).
- [2] Dragone, A., Caragiulo, P., Markovic, B., Herbst, R., Reese, B., Herrmann, S. C., Hart, P. A., Segal, J., Carini, G., Kenney, C. J., and Haller, G., "ePix: a class of architectures for second generation LCLS cameras," in [Journal of Physics: Conference Series], **493**, 012012, IOP Publishing (2014).
- [3] Markovic, B., Dragone, A., Caragiulo, P., Herbst, R., Nishimura, K., Reese, B., Herrmann, S., Hart, P. A., Blaj, G., Segal, J., Tomada, A., Hasi, J., Carini, G., Kenney, C., and Haller, G., "Design and characterization of the ePix100a prototype: a low noise integrating pixel ASIC for LCLS detectors," in [2014 IEEE Nuclear Science Symposium and Medical Imaging Conference (NSS/MIC)], 1–3, IEEE (Nov 2014).
- [4] Carini, G. A., Alonso-Mori, R., Blaj, G., Caragiulo, P., Chollet, M., Damiani, D., Dragone, A., Feng, Y., Haller, G., Hart, P., Hasi, J., Herbst, R., Herrmann, S., Kenney, C., Lemke, H., Markovic, B., Nelson, S., Nishimura, K., Osier, S., Pines, J., Robert, A., Segal, J., Sikorski, M., Song, S., Tomada, A., Weaver, M., and Zhu, D., "Studies of the ePix100 low-noise x-ray camera at SLAC," in [2014 IEEE Nuclear Science Symposium and Medical Imaging Conference (NSS/MIC)], 1–3, IEEE (Nov 2014).

- [5] Carini, G. A., Alonso-Mori, R., Blaj, G., Caragiulo, P., Chollet, M., Damiani, D., Dragone, A., Feng, Y., Haller, G., Hart, P., Hasi, J., Herbst, R., Herrmann, S., Kenney, C., Lemke, H., Manger, L., Markovic, B., Mehta, A., Nelson, S., Nishimura, K., Osier, S., Pines, J., Reese, B., Robert, A., Segal, J., Sikorski, M., Song, S., Thayer, J., Tomada, A., Weaver, M., and Zhu, D., “ePix100 camera: use and applications at LCLS,” *AIP Conference Proceedings* **1741**(1), 040008 (2016).
- [6] Blaj, G., Caragiulo, P., Carini, G., Dragone, A., Haller, G., Hart, P., Hasi, J., Herbst, R., Kenney, C., Markovic, B., Nishimura, K., Pines, J., Segal, J., Tamma, C., and Tomada, A., “Future of ePix detectors for high repetition rate FELs,” *AIP Conference Proceedings* **1741**(1), 040012 (2016).
- [7] Nishimura, K., Blaj, G., Caragiulo, P., Carini, G., Dragone, A., Haller, G., Hart, P., Hasi, J., Herbst, R., Herrmann, S., Kenney, C., Kwiatkowski, M., Markovic, B., Osier, S., Pines, J., Reese, B., Segal, J., Tomada, A., and Weaver, M., “Design and performance of the ePix camera system,” *AIP Conference Proceedings* **1741**(1), 040047 (2016).
- [8] Salvat, F., Fernández-Varea, J., and Sempau, J., [*PENELOPE-2011: A Code System for Monte Carlo Simulation of Electron and Photon Transport*], OECD Nuclear Energy Agency, Issy-les-Moulineaux, France (2011).
- [9] Trueb, P., Sobott, B. A., Schnyder, R., Loeliger, T., Schneebeili, M., Kobas, M., Rassool, R. P., Peake, D. J., and Broennimann, C., “Improved count rate corrections for highest data quality with PILATUS detectors,” *Journal of Synchrotron Radiation* **19**, 347–351 (May 2012).
- [10] Ballabriga, R., Aloyz, J., Blaj, G., Campbell, M., Fiederle, M., Frojdh, E., Heijne, E. H. M., Llopart, X., Pichotka, M., Procz, S., et al., “The Medipix3RX: a high resolution, zero dead-time pixel detector readout chip allowing spectroscopic imaging,” *Journal of Instrumentation* **8**(02), C02016 (2013).
- [11] Llopart, X., Ballabriga, R., Campbell, M., Tlustos, L., and Wong, W., “Timepix, a 65k programmable pixel readout chip for arrival time, energy and/or photon counting measurements,” *Nuclear Instruments and Methods in Physics Research Section A: Accelerators, Spectrometers, Detectors and Associated Equipment* **581**(12), 485 – 494 (2007). Proceedings of the 11th International Vienna Conference on Instrumentation.